

Determining Variability in Arctic Sea Ice Pressure Ridge Topography with ICESat-2

Kyle Duncan¹ and Sinead Louise Farrell²

¹Earth System Science Interdisciplinary Center

²University of Maryland

November 22, 2022

Abstract

We investigate the characteristics and distribution of pressure ridges in Arctic sea ice using surface height profiles from the Advanced Topographic Laser Altimeter System (ATLAS) on ICESat-2. Applying a new algorithm to ATLAS measurements we derive the frequency and height of individual pressure ridges and map surface roughness and ridging intensity at the basin scale over three winters between 2019 and 2021. Comparisons with near-coincident airborne lidar data show that not only can we detect individual ridges 5.6 m wide, but also measure sail height more accurately than the existing ICESat-2 sea ice height product. We find regional variability in ridge morphology is large while annual variability is low. Ridge characteristics are not only related to their parent ice type but also their geographic location. High-resolution satellite altimetry data are valuable for characterizing sea ice deformation at short length-scales, providing observations that will advance ridge parameterizations in sea ice models.

1 **Determining Variability in Arctic Sea Ice Pressure Ridge Topography with ICESat-2**

2
3 K. Duncan¹ and S. L. Farrell²

4
5 ¹Earth System Science Interdisciplinary Center, University of Maryland, College Park, MD,
6 USA.

7 ²Department Geographical Sciences, University of Maryland, College Park, MD, USA.
8

9 Corresponding author: Sinéad Louise Farrell (sineadf@umd.edu)

10
11 Farrell, Sinead Louise Orcid ID: 0000-0003-3222-2751

12 Duncan, Kyle Orcid ID: 0000-0001-6959-1206

13
14 *For Submission to Geophysical Research Letters*
15

16 **Key Points**

- 17 1. Advances in satellite laser altimetry techniques permit extensive mapping of pressure ridge
18 topography across the Arctic Ocean
- 19 2. Our methods detect individual ridges and produce ice deformation statistics at resolutions
20 previously only attainable with airborne lidar
- 21 3. As the oldest Arctic ice continues to decline, our results imply an on-going reduction in
22 ridging intensity and hence form drag over time
23

24 **Keywords**

- 25 • 0750 Sea ice
26 • 0758 Remote sensing
27 • 0774 Dynamics
28 • 0770 Properties
29
30

31 **Abstract**

32 We investigate the characteristics and distribution of pressure ridges in Arctic sea ice using surface
33 height profiles from the Advanced Topographic Laser Altimeter System (ATLAS) on ICESat-2.
34 Applying a new algorithm to ATLAS measurements we derive the frequency and height of
35 individual pressure ridges and map surface roughness and ridging intensity at the basin scale over
36 three winters between 2019 and 2021. Comparisons with near-coincident airborne lidar data show
37 that not only can we detect individual ridges 5.6 m wide, but also measure sail height more
38 accurately than the existing ICESat-2 sea ice height product. We find regional variability in ridge
39 morphology is large while annual variability is low. Ridge characteristics are not only related to
40 their parent ice type but also their geographic location. High-resolution satellite altimetry data are
41 valuable for characterizing sea ice deformation at short length-scales, providing observations that
42 will advance ridge parameterizations in sea ice models.

43

44 **Plain Language Summary**

45 Pressure ridges, a result of convergence and deformation between ice floes, restrict the movement
46 of air across sea ice and pose an impediment to transport across or through the ice by humans,
47 animals or marine vessels. The laser altimeter on ICESat-2 provides height measurements of sea
48 ice surface topography every 0.7 m in the direction of flight, from which we calculate surface
49 roughness and measure the sail height and frequency of pressure ridges across the Arctic. We use
50 coincident aircraft-mounted lidar data to evaluate the accuracy of ridge topography derived from
51 ICESat-2. We show that our methods accurately distinguish ridges and reproduce sea ice
52 deformation statistics at an along-track resolution previously only attainable from airborne
53 platforms. We find that while year-to-year variability in pressure ridge morphology is low, regional
54 variations are significant. In agreement with previous studies, we find distinct deformation
55 characteristics depending on the parent ice type. The results demonstrate that high-resolution
56 satellite altimeter observations can be used to derive detailed measurements of sea ice topography
57 that will ultimately support process studies and advances in sea ice modeling.

58

59 **1 Introduction**

60 The advent of high-resolution satellite laser altimetry permits for the first time a complete
61 mapping of sea ice surface topography at the basin scale. The Advanced Topographic Lidar

62 Altimeter System (ATLAS) on ICESat-2 has a footprint on Earth’s surface approximately 11 m in
63 diameter (Magruder et al., 2020), and a high pulse repetition frequency of 10 kHz, resulting in
64 oversampled footprints at ~0.7 m along-track (Markus et al., 2017). This sampling configuration
65 is ideal for mapping rough sea ice surface topography in high fidelity year round, allowing us to
66 resolve individual ice floes, pressure ridges and leads at meter-scale (Farrell et al., 2020). This
67 marks a significant advance in our capabilities for observing ice deformation compared to previous
68 techniques, including airborne laser profiling (e.g., Hibler et al., 1974; Lowry and Wadhams, 1979;
69 Wadhams et al., 1992; Dierking, 1995; Tan et al., 2012), upward looking and side scan sonar (e.g.,
70 Hibler et al., 1972; Davis and Wadhams, 1995), autonomous underwater vehicles (e.g., Wadhams
71 and Doble, 2008), airborne electromagnetic induction techniques (Martin, 2007; Haas et al., 2009),
72 and in situ observations (e.g., Timco and Burden, 1997; Strub-Klein and Sudom, 2012), that were
73 each spatiotemporally limited. Leveraging widespread ICESat-2 observations, we extract the
74 morphological characteristics of sea ice ridges across the Arctic Ocean and examine variations in
75 ridging as a function of geographical area.

76 Pressure ridges that are formed through convergence increase ice thickness. They impact
77 atmospheric flow across the ice surface and modify the momentum flux from the atmosphere
78 through the ice to the ocean (Arya, 1973). Defined as a wall of broken ice forced up by pressure
79 (WMO, 1970), ridges can be “fresh” (i.e., a first-year ridge) or “weathered and old”. The sail, the
80 portion above the local sea surface, consists of blocks of ice piled up and frozen together by
81 contact, often with open voids. The submerged volume of broken ice, forced downwards by
82 pressure, is termed an ice keel. Pressure ridges in isostatic equilibrium mature to roughly triangular
83 sails with rounded crests (Parmerter and Coon, 1972). Early submarine observations revealed an
84 uneven distribution of ridging across the Arctic with the heaviest deformation found north of
85 Greenland and the Canadian Arctic Archipelago (e.g., Hibler et al., 1974; Bourke and McLaren,
86 1992).

87 Knowledge of sea ice topography is necessary to parameterize momentum transfer to the
88 ocean in numerical simulations since surface stress increases with surface roughness (Martin et al.,
89 2016; Tsamados et al., 2014). The roughness of the sea ice accumulates, and persists, throughout
90 the growth season and, depending on the location of the ice, can potentially survive dissipation
91 through melt or advection. Multiyear ice that has survived at least one summer melt season is
92 hence rougher than first-year ice (Wadhams and Toberg, 2012). A form drag parameterization

93 based on direct observations of roughness (Tsamados et al., 2014) demonstrated both regional and
94 temporal variability in form drag, and when implemented, resulted in a net decline in ice thickness,
95 area and velocity compared to the model control run. Variability and trends in ice surface
96 roughness due to the sustained multi-decadal loss of older ice (Perovich et al., 2019) are not
97 adequately represented in sea ice models (Martin et al., 2016). Ridge metrics are also required for
98 modeling the design load of sea ice on marine structures such as oil rigs and vessels (Timco and
99 Burden, 1997) and the scattering of under-ice acoustics (Wadhams and Toberg, 2012).

100 Sea ice roughness is used here as a general term to describe all sources of ice deformation
101 through ridging, rafting and rubbling, and includes hummocks as well as wind-driven undulations
102 on the ice surface due to snowdrifts and sastrugi. Due to its dense along-track sampling, ICESat-2
103 has the capability to directly observe ice deformation at the scale of the individual pressure ridge.
104 We can therefore retrieve ridge morphology. Here we calculate the standard deviation of surface
105 elevation to estimate surface roughness (σ_h) and we characterize the upper expression of pressure
106 ridges (sails) to obtain estimates of sail height (H_S) as well as ridge width (W_R), spacing (D_R) and
107 intensity (I_R). We investigate regional variations at the end of winter (April) over three years
108 between 2019 and 2021. Our derived statistics represent deformation accumulated throughout the
109 winter period and hence include both fresh and weathered ridges. We analyze ridge morphology
110 at different length scales, ranging from individual floes, to regional-scale deformation relevant for
111 climate modelling, and upwards to the full basin scale, providing pan-Arctic metrics. Statistical
112 models fit to the observations describe the characteristic shapes of the derived ridge dimensions in
113 two regions with distinct ice deformation history. Our results are validated via comparison with
114 near coincident Operation IceBridge (OIB) lidar data, collected during direct under-flights of
115 ICESat-2 in April 2019.

116

117 **2 Data and Methods**

118

119 **2.1 ATL03**

120 Over sea ice, ATLAS (operating at 532 nm) obtains multibeam surface height profiles of
121 the air/snow interface with respect to the reference ellipsoid (see e.g., Kwok et al., 2019b for
122 further details). The ICESat-2 ATL03 global geolocated photon height data product (Neumann et
123 al., 2021) is designed to be a single source for all photon data and ancillary information needed for

124 higher-level ICESat-2 data processing. ATL03 contains the latitude, longitude and height (h_{ph})
125 relative to the WGS-84 ellipsoid of all photons downlinked by the ATLAS instrument. The
126 ATLAS pulse width of 1.5 ns results in photon height uncertainty of ~ 0.23 m (Kwok et al., 2019b).

127

128 **2.2 ATL07**

129 The ICESat-2 ATL07 sea ice height data product (Kwok et al., 2021) is derived from the
130 ATL03 product. It contains sea ice and lead heights, adjusted for geoid and tidal variations and
131 inverted barometer effects. It is calculated using 150-photon height aggregates in segments with
132 variable lengths in the along-track direction ranging from ~ 27 m to 200 m and has a height
133 precision of ~ 0.02 m over flat surfaces such as leads (Kwok et al., 2019b).

134

135 **2.3 Ridge detection**

136 The number of photons recorded by the ATLAS detector depends on both the morphology
137 and reflectance of Earth's surface. Detections comprise photons scattered from the surface (signal)
138 and background (noise) photons, including from solar background, detector noise and photons
139 scattered by the atmosphere. The separation of background from surface photons is thus a critical
140 step in the retrieval of accurate surface height profiles.

141 Kwok et al. (2019a) report that the ATL07 algorithm, which uses a fixed 150-photon
142 aggregate designed for surface finding in the complex ice cover, does not capture the variability
143 of the sea ice height distribution at short length-scales in areas of high surface roughness where
144 pressure ridges are present. Since our goal is to retrieve pressure ridge topography, we must
145 therefore apply a novel method that takes advantage of the full-resolution geolocated photon
146 heights in the ATL03 product. The University of Maryland-Ridge Detection Algorithm (UMD-
147 RDA) is designed to extract sea ice surface height, h , from ATL03 data. Over sea ice, ATL03
148 provides photon heights (h_{ph}) in a 30 m vertical window that includes the surface return. We
149 construct a h_{ph} height distribution with a vertical bin size of 0.5 m and use a 5-shot horizontal
150 aggregate (~ 2.8 m along-track distance). Photons clustered around the mode of the h_{ph} distribution
151 are associated with the surface return and these are retained. If the h_{ph} distribution is bimodal, with
152 modes in consecutive bins, the lowest mode is selected to indicate the surface mode (h_m). For
153 bimodal h_{ph} distributions with modes that do not occur in consecutive bins, modal heights are
154 compared with those of the previous shot and the mode closest to the previous modal height is

155 selected to indicate h_m . Only photons within the range $(h_m + 10 \text{ m}) \geq h_{ph} \geq (h_m - 2 \text{ m})$ are retained
156 so as to adequately capture h_{ph} of ridge sails and leads, respectively. All other photons are
157 considered background photons and are discarded. To reduce any remaining background photons
158 from the final derivation of h , photons are further down selected, retaining only those within the
159 15th – 85th percentiles of the h_{ph} distribution. Sea ice surface height (h) is defined as the 99th
160 percentile of the remaining h_{ph} distribution and indicates the retrieval arising from the air/snow
161 interface, i.e., the first surface interface encountered by the laser pulse.

162 The UMD-RDA surface finding approach is applied on a per-shot basis to retain h at a
163 maximum along-track resolution of ~ 0.7 m. UMD-RDA height estimates are however only
164 processed where ATL07 data are available (Kwok et al., 2021) and hence not produced for cloud-
165 contaminated retrievals. Atmospheric, tide, and mean sea surface (MSS) geophysical height
166 corrections are applied to h so as to obtain corrected heights (h_c) relative to the MSS. Here we use
167 the Technical University of Denmark 2018 Mean Sea Surface (DTU18 MSS) model (Andersen et
168 al., 2018). Ice surface roughness (σ_h) is estimated by taking the standard deviation of h_c in 25 km
169 along-track segments for all cloud-free ICESat-2 sea ice data north of 65°N.

170 Next, the morphological characteristics of individual ridge sails on the ice surface are
171 determined. The local level ice surface (H_L) is computed as the mode of the h_c height distribution
172 in 25 km along-track segments. In segments with a large percentage of leads, the h_c distribution
173 can be bimodal. In these cases, the highest modal elevation defines H_L . So as to extract ridge
174 heights, all estimates of h_c are converted to height anomalies (h_a) relative to H_L . ICESat-2 has the
175 capability to observe the surface topography of all floating morphological features of the ice cover
176 that are larger than the minimum resolution, including ridges, rafts, rubble fields and hummocks
177 as well as sastrugi and snowdrifts. Since our goal is to detect and characterize pressure ridges, we
178 set an optimal cutoff height (H_0) above H_L , that defines the minimum ridge height (Lowry and
179 Wadhams, 1979). Here, $H_0 = 0.6$ m (following Hibler et al., 1972; Duncan et al., 2018) and thus
180 differentiates ridge sails from other surface features such as sastrugi. Independent ridges are
181 defined using the Rayleigh criterion where the local maximum (peak) is at least twice as high as
182 the neighboring minima (troughs) on both sides and the minima descend at least halfway toward
183 H_L (Lowry and Wadhams, 1979; Tan et al., 2012). Independent ridges can therefore comprise
184 multiple sails, and two adjacent topographical elements must fulfill the Rayleigh criterion to be
185 resolved as separate ridge elements (Castellani et al., 2014). H_s is the maximum sail height of a

186 ridge relative to H_L (i.e., the maximum h_a within the ridge element). Following Timco and Burden
187 (1997), ridge width (W_R) is measured as distance in the along-track direction between the points
188 of intersection of H_L and the neighboring minima on either side of the ridge peak. Ridge spacing
189 (D_R) is the peak-to-peak distance between consecutive H_S maxima. The latter two metrics will be
190 impacted by the angle of intersection between the ICESat-2 orbit and the ridge orientation, but
191 assuming heterogeneity in ice surface conditions across the Arctic, they should be robust at the
192 basin scale.

193

194 **2.4 Validation Data**

195 ICESat-2's capabilities to measure sea ice surface topography in high resolution are
196 quantified through comparisons of both the UMD-RDA and ATL07 sea ice heights with coincident
197 aircraft observations. We use Airborne Topographic Mapper (ATM) lidar data (Studinger, 2020)
198 collected during under-flights of ICESat-2 in April 2019 as part of NASA's OIB campaign
199 (MacGregor et al., 2021). Analyzing these data, Kwok et al. (2019a) found that ATM and ATL07
200 surface height profiles were highly correlated when ATM data were averaged at the ATL07
201 segment length scale ($\sim 27 - 200$ m) and manually coregistered. Larger differences were however
202 found in areas of rough sea ice, when the ATL07 algorithm was unable to capture the full height
203 distribution due to the segment-based approach (Kwok et al., 2019a).

204 Here we examine airborne observations from two underflights that had spatiotemporal
205 coincidence with ICESat-2 orbits. On 19 April, 2019, ~ 142 km of coincident validation data were
206 collected below ICESat-2 reference ground track (RGT) 325, while on 22 April, 2019 coincident
207 data spanning ~ 233 km were collected below RGT 371. Since the ATM is a conically-scanning
208 lidar (Krabill et al., 2002) it samples the ice surface unevenly (Duncan et al., 2018). We
209 investigated the averaging length best suited for validation of the finer-scale ICESat-2 observations
210 (Duncan et al., 2020), and here ATM data are extracted along the ICESat-2 height profiles using a
211 $n=5$ nearest neighbor mean. UMD-RDA, ATL07 and ATM height profiles relative to the DTU18
212 MSS are sampled at 10 m along-track increments for direct comparison.

213

214 **3 Kilometer-Scale Topography**

215 First, we examine sea ice height at the floe scale $O(1-10$ km). We compare measurements
216 of h_c derived from ATM, ATL07 and the UMD-RDA (Figure 1). The validation site (Figure 1c)

217 comprised the oldest, thickest sea ice in the Arctic (Perovich et al., 2019). The height variability
218 of this heavily deformed surface (Figure 1a) is captured by all three methods. At the km-scale
219 (Figure 1b) we can see both individual small ridges with a typical triangular shape in cross-section
220 as well as the structure of ridge complexes, with multiple sails and irregular height profiles.
221 Pressure ridge (H_s , W_R , D_R) and surface topography metrics (H_L and H_θ) described in Section 2.3
222 are illustrated in Figure 1b.

223 Comparisons against ATM data show that the ATL07 algorithm acts as a low-pass filter,
224 underestimating the height of individual ridge sails (red curves, Figures 1a, b), consistent with
225 previous studies (Kwok et al., 2019a). Despite this, ATL07 heights are strongly correlated with
226 ATM heights ($r \geq 0.82$, red dots, Figures 1d and e). They are however biased low by ~ 0.12 m, with
227 median height underestimated by 0.06 – 0.08 m (Figures 1f and g). The largest differences are
228 associated with rougher ice topography (Figures 1d-g).

229 UMD-RDA is designed to resolve individual ridges in the full-resolution photon data and
230 the resulting height distributions are strongly correlated with ATM heights ($r \geq 0.86$, blue dots,
231 Figures 1d and e). ATM and UMD-RDA mean, median and modal heights differ by ≤ 0.02 m
232 (Figures 1f and g). Examining UMD-RDA heights across the central Arctic (ATL03 segment 04,
233 Figure 1c), 3936 ridges are detected on RGT #325, and 5723 on RGT #371. The narrowest ridge
234 resolved is 5.6 m wide. Modal ridge width is 35 m, and median and mean widths are ~ 71 m and
235 ~ 90 m, respectively (Figure 1h and i).

236

237 **4 Interannual Variability at Pan-Arctic Scales**

238 To investigate the regional gradients in ice roughness and their interannual variability, σ_h
239 in April 2019 – 2021 is mapped at $1/4^\circ$ across the Arctic Ocean (Figure 2). The σ_h distribution
240 histograms (insets, Figure 2) show little change in mean σ_h during the three-year period, which
241 ranges 0.25-0.27 m. The maps however illustrate the dichotomy in σ_h between ice types, where
242 the convergent ice regimes north of Greenland and Ellesmere Island result in the majority of
243 multiyear ice with $\sigma_h \geq 0.3$ m, while first-year ice has $\sigma_h \leq 0.2$ m. Figure 2 also reveals advection
244 of multiyear ice through the southern Beaufort Sea, which was particularly prevalent in April 2021
245 and the loss of multiyear ice through the Fram Strait.

246 Extending the analysis to the derived ridge metrics provides further insight into the state
247 of the sea ice cover and the year-to-year variations in Arctic ice deformation. Here, H_{Smax} is the

248 maximum H_S per kilometer, while D_R is defined as the mean ridge spacing per 10 km. As with σ_h ,
249 these data are also mapped to a $1/4^\circ$ grid. Regional variability in D_R does not directly map to H_{Smax}
250 and hence a metric combining these variables is useful. Ridging intensity (I_R), first introduced by
251 Hibler et al. (1974), is easily derived from laser profiling data and is defined as the mean sail height
252 multiplied by the sail frequency per kilometer (i.e., $I_R = \langle H_S \rangle / \langle D_R \rangle$, where $\langle H_S \rangle$ is mean sail
253 height and $\langle D_R \rangle$ is mean spacing). I_R is proportional to aerodynamic form drag of pressure ridges
254 (Arya, 1973; Dierking, 1995). Figure 2 reveals that I_R is correlated with σ_h . Both metrics indicate
255 higher than normal ridged ice along the Siberian coastline, particularly in the southwestern
256 Chukchi Sea, East Siberian Sea and Laptev Sea. This localized ice deformation could be due to
257 convergence against a land boundary or land-fast sea ice.

258

259 **5 Regional-Scale Ice Deformation**

260 Bridging between the kilometer and pan-Arctic scales (Figures 1 and 2) we analyze
261 ICESat-2 data at the intermediate scale $O(10 - 100 \text{ km})$, relevant to the typical resolution of climate
262 models (Hunke et al., 2010). Pressure ridge distributions from two parts of the Arctic Ocean are
263 compared: north of the Canadian Arctic Archipelago, region A encompasses older, rougher,
264 thicker, mainly multi-year sea ice, while region B lies within the Beaufort Gyre encompassing
265 younger, smoother, predominantly first-year ice. These two distinct regions were selected by
266 examining the geographical distribution of σ_h between April 2019 and 2021 (Figure 2). Their areas
267 are approximately equal so that the number of observations between the two regions is equivalent.

268 We calculate the distributions of σ_h , H_{Smax} and D_R in A and B and investigate the best
269 statistical fits to these distributions. The regional results (Figure 3) show that all distributions have
270 exponential tails denoting the fraction of pressure ridging present. Differences in ice deformation
271 between the two regions are however apparent. In region A, average σ_h was $\sim 0.4 \text{ m}$ but decreased
272 by 0.04 m over the three-year period (Figure 3a), while in region B, mean and modal σ_h remained
273 approximately constant at $\sim 0.2 \text{ m}$ during the study period (Figure 3g). Surface height variability
274 was larger in region A and the standard deviation of σ_h was approximately double that of region
275 B (Figures 3a and g). The elongated tail of the H_{Smax} distribution in region A (Figure 3b) reveals
276 that sails are frequently thicker than 3 m in older ice, but this is rare in younger ice (region B,
277 Figure 3h). The data confirm that smaller ridges are more common across the ice cover than very

278 large, pressure ridge complexes (Figures 3b and h). Roberts et al. (2019) explained this
279 theoretically, demonstrating that deformation of the ice cover seldom makes it to the later stages
280 of ridging and that most sea ice is minimally crushed when the pack is compressed, since it is
281 energetically preferable to form many small ridges rather than few large ridges. H_{Smax} in the older
282 ice of region A averaged 0.63-0.72 m higher than in region B and modal H_{Smax} was approximately
283 double that of region B (Figures 3b and h). 5% of sails in region A were ≥ 3.12 m, with 1 % of
284 sails ≥ 4 m, while 95 % of all sails in region B were ≤ 2 m. Ridge sails were 2.6-2.8 times further
285 apart in region B than in region A, with modal D_R of 375-475 m in region B compared to 125-225
286 m in region A (Figures 3c and i).

287 The non-Gaussian nature of the sea ice surface height distribution is demonstrated in
288 Figures 3d and j, where σ_h observations are well fit by an exponential normal (exponentially
289 modified Gaussian distribution) model in both regions, though the positively skewed surface
290 topography is more evident in the older ice zone of region A. The statistical distribution of H_{Smax}
291 in region A is best represented by a log-normal distribution (Figure 3e) and the tail is almost
292 straight on the semi-log axis, indicating a negative exponential tail also commonly observed in ice
293 thickness distributions (e.g., Haas et al., 2010). The H_{Smax} distribution in region B has not however
294 acquired a fully negative exponential tail, and these data were also well represented by a Weibull
295 distribution (not shown). Previous studies have shown D_R follows a log-normal distribution (e.g.,
296 Davis and Wadhams, 1995; Dierking, 1995). Our observations of D_R are best fit by a log-logistic
297 distribution in regions A and B (Figures 3f and l) similar in shape to a log-normal distribution but
298 with heavier tails. The results show a slight increase in D_R in both regions between April 2019 and
299 2021 suggesting less frequent ridging over time.

300

301 **6 Discussion**

302 ICESat-2 measurements of ice surface topography can reproduce sea ice deformation
303 statistics at a resolution previously only attainable from aircraft surveys. Sea ice surface roughness
304 (σ_h), sail height (H_{Smax}), ridge width (W_R), spacing (D_R) and intensity (I_R), measured at the end of
305 winter between 2019 and 2021, yielded good coverage across a range of ice types and deformation
306 regimes in the Arctic Ocean. Comparing the amount of topographic data assessed here with the
307 published literature, we believe this is the largest ice deformation data set of its kind created to
308 date (Duncan & Farrell, 2022). The ongoing availability of ICESat-2 data offers the possibility to

309 monitor σ_h year-round, map regional deformation events, derived from individual pressure ridges,
310 soon after their occurrence, and track seasonal and interannual variability.

311 Building upon initial results presented in Farrell et al. (2020), we investigated ridge
312 topography at a range of length scales $O(1 - 1000 \text{ km})$. Consistent with previous studies (e.g.,
313 Hibler et al., 1974; Bourke and McLaren, 1992; Wadhams and Toberg, 2012) our results show that
314 ice deformation is much more prevalent in multi-year ice zones than in seasonal areas. Our results
315 also confirm that deformation varies not only with ice regime, but also with geographic location.
316 Both H_{Smax} and I_R are greatest along the land boundaries of the multi-year ice zone and can be a
317 factor of two larger than the deformation characteristics of multi-year ice at more northerly
318 latitudes in the central Arctic. Localized deformation in the seasonal ice zone, due to convergence
319 against a land boundary, can result in areas with I_R commensurate with that found in multi-year
320 ice. H_{Smax} was well represented by a log-normal distribution in both rough and smooth ice regimes,
321 but H_{Smax} was $>60\%$ larger in the roughest ice zone with little interannual variability across the
322 three years studied. In the smoother ice zone, D_R was 2-3 times greater than in the rougher ice.
323 H_{Smax} and I_R were lower overall in April 2021 than in 2019 and 2020, especially in the Eurasian
324 Basin.

325 Although knowledge of pressure ridge characteristics such as H_S , D_R and I_R is necessary to
326 model form drag, this information remains lacking in many Earth system models (Tsamados et al.,
327 2014; Martin et al., 2016; Roberts et al., 2019). Martin et al. (2016) showed that such models lack
328 a complete representation of feedbacks between ice roughness, thickness, drift and deformation,
329 limiting the prediction of atmosphere-ice-ocean momentum transfer and how it varies with time.
330 Roberts et al. (2019) suggest that pressure ridge observations are required to accurately model ice
331 pack roughness and they propose that individual ridge statistics may be used to derive the evolution
332 of the ice thickness distribution. ICESat-2 delivers observations of both individual pressure ridges
333 at the scale of a model grid cell and σ_h and I_R at the basin scale thereby providing the needed ice
334 deformation statistics to advance sea ice parameterizations.

335 First-year ice now comprises $\sim 70\%$ of the Arctic ice cover, compared to 35-50% in the
336 1980s (Perovich et al., 2019). As the Arctic rapidly transitions to a predominantly first-year ice
337 cover with the continued loss of the oldest ice (Tschudi et al., 2020), ice topography will become
338 dominated by the characteristics of pressure ridges in seasonal ice (Wadhams and Toberg, 2012).
339 The sustained loss of multi-year ice, coupled with our basin-scale results, implies a decline in H_S ,

340 an increase in D_R and an on-going reduction in I_R and hence form drag over time. Long-term and
341 widespread observations of ice deformation from ICESat-2 will improve our understanding of how
342 sea ice moderates the momentum flux between the atmosphere and ocean, providing a more
343 complete picture of how and why the ice regime of the Arctic Ocean is transforming.

344

345 **Data Availability Statement**

346 NASA ICESat-2 ATL03 data are available at <https://doi.org/10.5067/ATLAS/ATL03.005> and
347 ATL07 sea ice height data are available at <https://doi.org/10.5067/ATLAS/ATL07.005>. NASA
348 ATM data are available at <https://doi.org/10.5067/19SIM5TXKPGT>. The DTU18 MSS is
349 available at <https://ftp.space.dtu.dk/pub/DTU18/>. Processed sea ice pressure ridge sail data
350 described in this manuscript are available at <https://doi.org/10.5281/zenodo.6772545>.

351

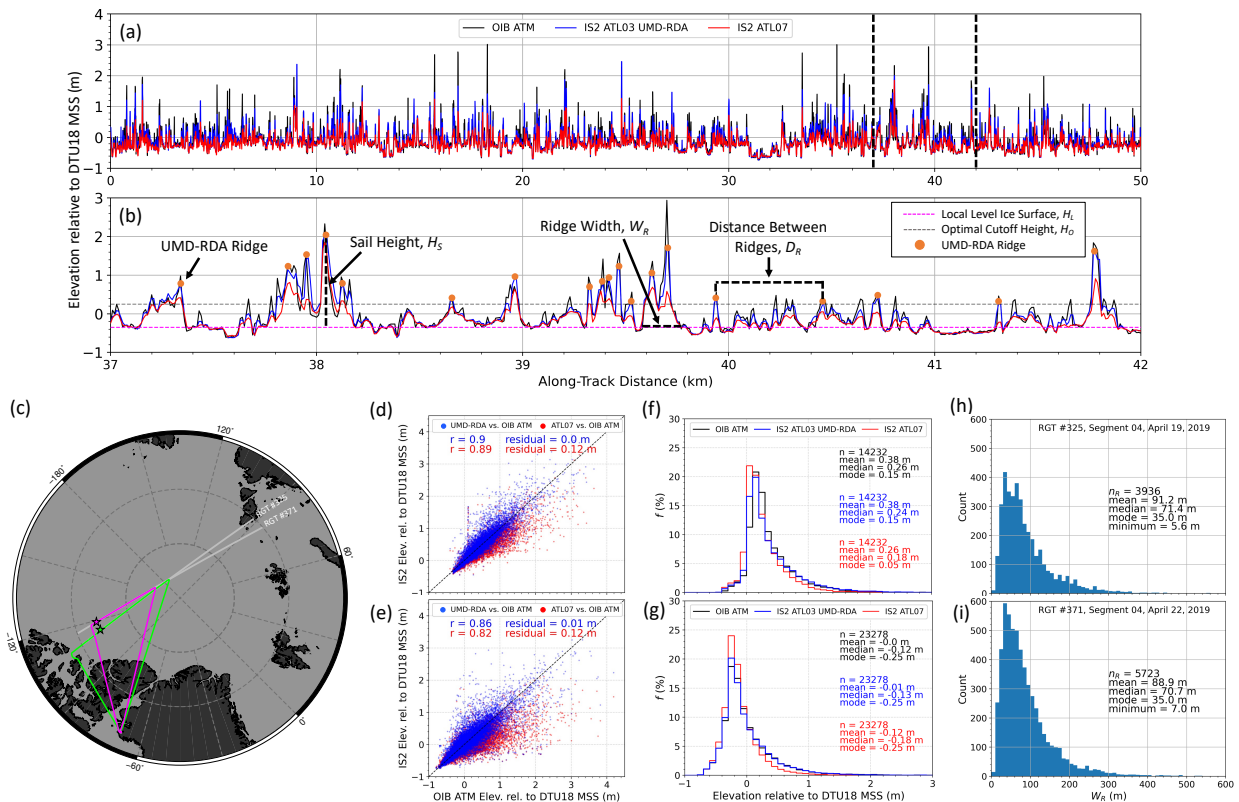
352 **Acknowledgements**

353 This study is supported under NASA Cryosphere Program Grant 80NSSC20K0966 (ICESat-2
354 Science Team). The authors thank Jennifer Hutchings, Jacqueline Richter-Menge and Andrew
355 Roberts for their useful discussions and thoughtful advice while we conceived and performed this
356 study. We thank the ICESat-2 and IceBridge teams for processing the data used here.

357

358 **Figures**

359

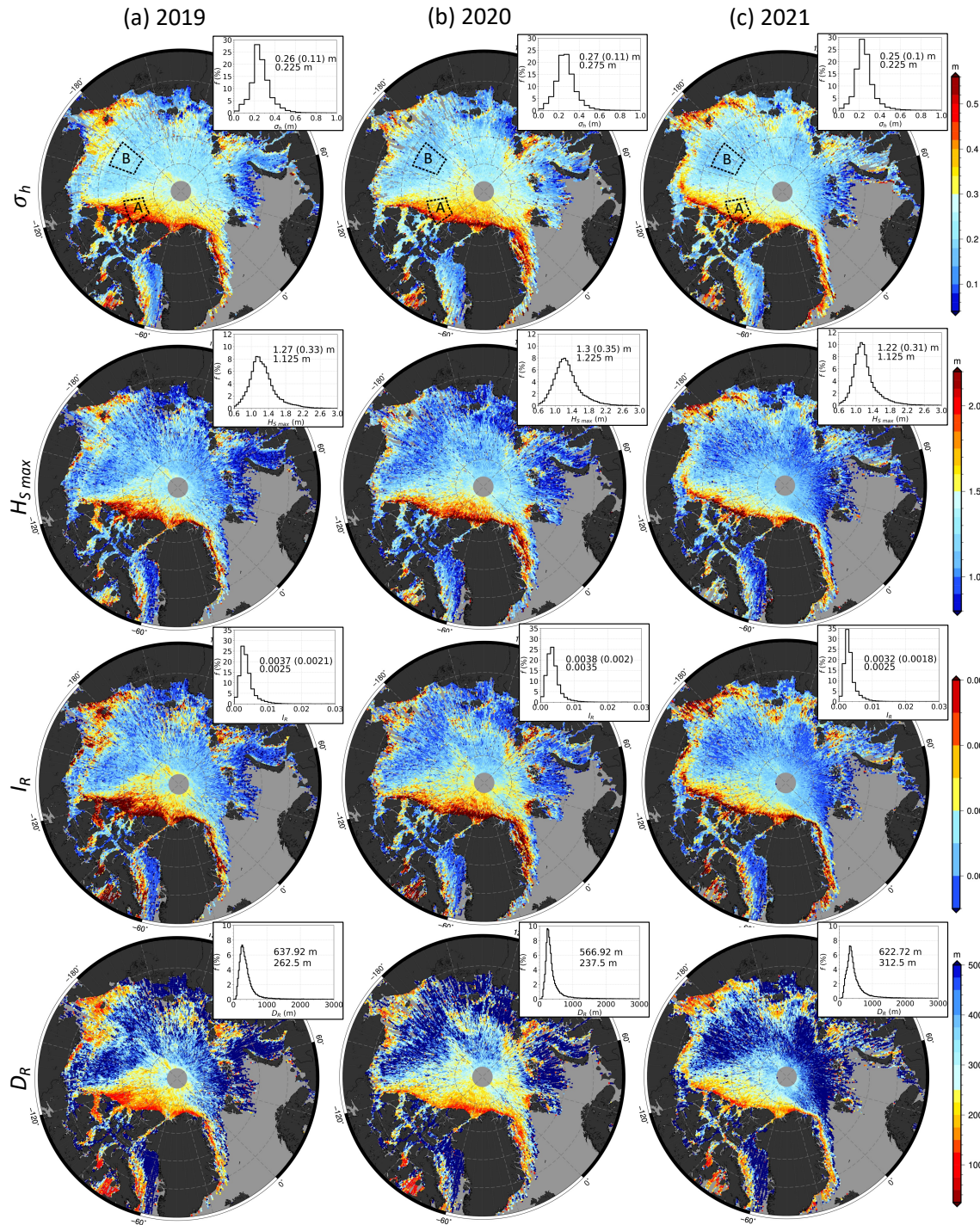


360

361

362 **Figure 1.** Arctic sea ice topography from ICESat-2. (a) OIB ATM airborne lidar (black), ICESat-
 363 2 ATL03 UMD-RDA (blue) and ATL07 (red) sea ice height profiles along a 50 km transect across
 364 multi-year sea ice (location indicated by magenta star in c) on 22 April, 2019. (b) A close-up 5-
 365 km view (section between vertical black dashed lines in a) illustrating surface topography and
 366 pressure ridge metrics defined in the text. (c) Map showing OIB flights on 19 (green) and 22
 367 (magenta) April, 2019, with segment 04 of ICESat-2 reference ground tracks (RGTs) 325 and 371
 368 (gray lines) and the locations of coincident validation data collection (stars). (d, e) Scatterplots
 369 comparing UMD-RDA (blue dots) and ATL07 (red dots) surface heights with coincident OIB
 370 ATM height measurements on 19 and 22 April, 2019, respectively. (f, g) Sea ice surface height
 371 distributions for coincident OIB ATM (black), UMD-RDA (blue), and ATL07 (red) data on 19
 372 and 22 April, 2019, respectively. (h, i) Ridge width distributions derived from ALT03 segment 04
 373 of RGTs 325 and 371, respectively, using the UMD-RDA.

374

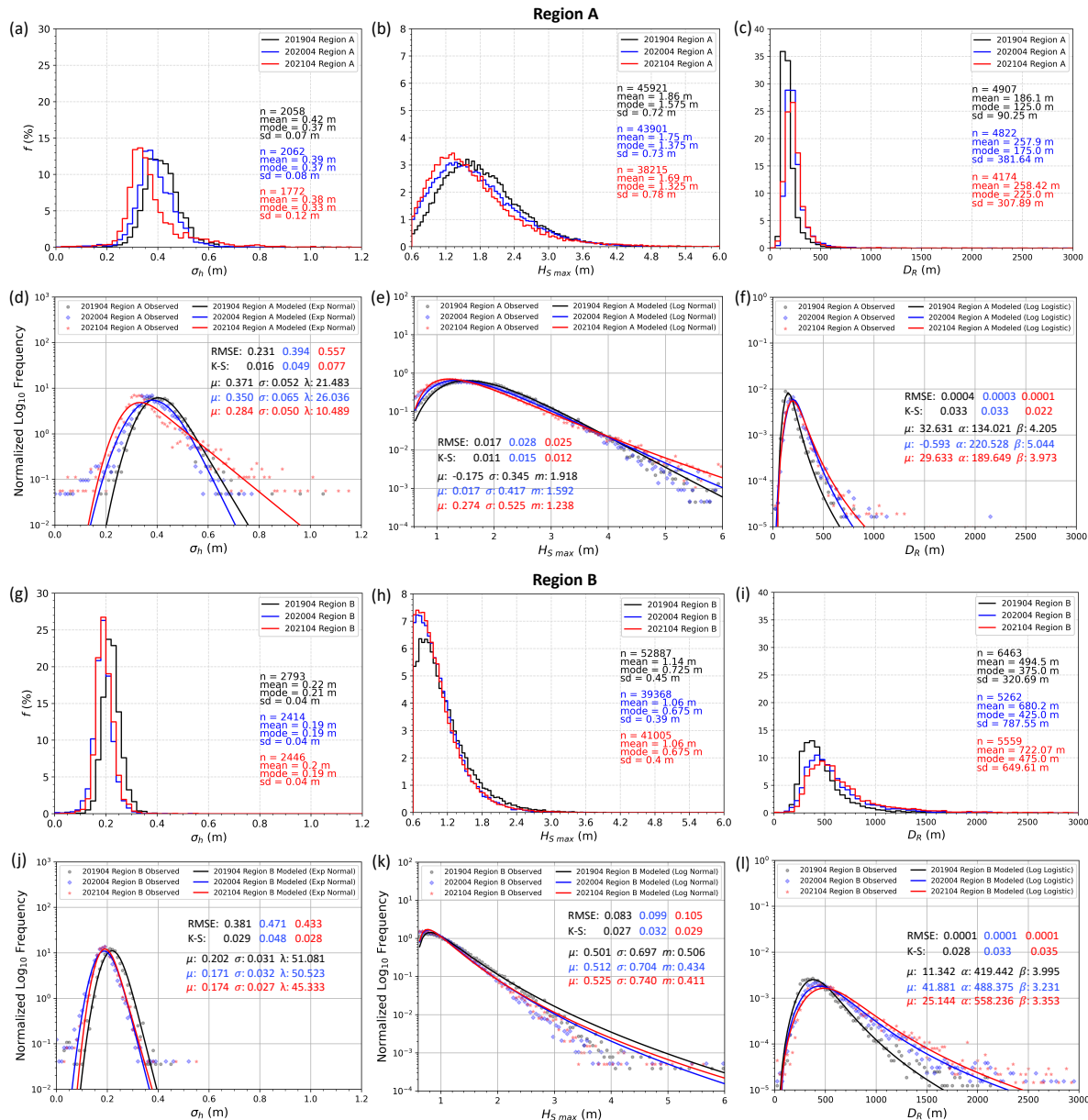


375

376

377 **Figure 2.** Pan-Arctic maps of surface roughness (σ_h), maximum sail height (H_{smax}), ridge intensity
 378 (I_R), and distance between ridges (D_R) in April (a) 2019, (b) 2020 and (c) 2021. Insets show the
 379 histogram distributions with mean (standard deviation) and modal statistics provided to the right

380 of each histogram. Dashed black lines (top row) outline the locations (A, B) of the regional analysis
 381 described in the text.
 382



383
 384
 385 **Figure 3.** Statistical analysis of surface roughness (σ_h), maximum sail height (H_{Smax}) and distance
 386 between ridges (D_R) in April 2019 (black), 2020 (blue) and 2021 (red) for regions A (a – f) and B
 387 (g – l). Distributions of σ_h , H_{Smax} and D_R with the number of observations (n) and their mean, mode
 388 and standard deviation (sd) are shown on rows 1 and 3, for regions A and B, respectively. Semi-

389 log plots of σ_h , H_{Smax} and D_R and their model fits are on rows 2 and 4, for regions A and B,
390 respectively. Root-mean-square error (RMSE), Kolmogorov–Smirnov (K-S) test statistics and the
391 model parameters are shown to the right of each distribution.

392

393 **References**

394 Andersen, O. B., Rose, S. K., Knudsen, P. & Stenseng L. (2018). The DTU18 MSS Mean Sea
395 Surface improvement from SAR altimetry. Technical University of Denmark, Copenhagen,
396 Denmark.

397 https://ftp.space.dtu.dk/pub/DTU18/MSS_MATERIAL/PRESENTATIONS/DTU18MSS-V2.pdf

398

399 Arya, S. P. S. (1973). Contribution of form drag on pressure ridges to the air stress on Arctic ice.

400 *J. Geophys. Res.*, 78(30), 7092–7099.

401

402 Bourke, R. H., and McLaren, A. S. (1992). Contour mapping of Arctic basin ice draft and

403 roughness parameters. *J. Geophys. Res.*, 97(C11), 17715– 17728, doi:10.1029/92JC01857.

404

405 Castellani G., Lupkes, C., Hendricks, S., & Gerdes, R. (2014). Variability of Arctic sea ice

406 topography and its impact on the atmospheric surface drag. *J. Geophys. Res. Oceans*, 119, 6743–

407 6762.

408

409 Davis, N. R., & Wadhams, P. (1995). A statistical analysis of Arctic pressure ridge morphology.

410 *Journal of Geophysical Research*, 100(C6), 10,915–10,925. <https://doi.org/10.1029/95JC00007>

411

412 Dierking, W. (1995). Laser profiling of the ice surface topography during the Winter Weddell

413 Gyre Study 1992. *J. Geophys. Res.*, 100(C3), 4807– 4820, doi:10.1029/94JC01938.

414

415 Duncan, K., & Farrell, S. L. (2020). High-Resolution Sea Ice Topography from ICESat-2. *Earth*

416 *and Space Science Open Archive*, 1. <https://doi.org/10.1002/essoar.10505000.1>

417

418 Duncan, K. & Farrell, S. (2022). ICESat-2 Arctic Sea Ice Surface Topography from the University
419 of Maryland-Ridge Detection Algorithm: April 2019, 2020, and 2021 (Version 1) [Data set].
420 Zenodo. <https://doi.org/10.5281/zenodo.6772545>
421

422 Duncan, K., Farrell, S. L., Connor, L. N., Richter-Menge, J., & Dominguez, R. (2018). High-
423 resolution airborne observations of sea ice pressure-ridge sail height. *Annals of Glaciology*,
424 *59*(76pt2), 137–147. <https://doi.org/10.1017/aog.2018.2>.
425

426 Duncan, K., Farrell, S. L., Hutchings, J., & Richter-Menge, J. (2020). Late Winter Observations
427 of Sea Ice Pressure Ridge Sail Height. *IEEE Geoscience and Remote Sensing Letters*.
428 <https://doi.org/10.1109/LGRS.2020.3004724>.
429

430 Farrell, S. L., Duncan, K., Buckley, E. M., Richter-Menge, J., & Li, R. (2020). Mapping Sea Ice
431 Surface Topography in High Fidelity with ICESat-2. *Geophysical Research Letters*, *47*,
432 e2020GL090708. <https://doi.org/10.1029/2020GL090708>.
433

434 Haas, C., Hendricks, S., Eicken, H., & Herber, A. (2010). Synoptic airborne thickness surveys
435 reveal state of Arctic sea ice cover, *Geophys. Res. Lett.*, *37*, L09501, doi:10.1029/2010GL042652.
436

437 Haas, C., Lobach, J., Hendricks, S., Rabenstein, L., & Pfaffling, A. (2009). Helicopter-borne
438 measurements of sea ice thickness, using a small and lightweight, digital EM system. *Journal of*
439 *Applied Geophysics*, *67*(3), 234-241.
440

441 Hibler III, W. D., Weeks, W. F., & Mock, S. J. (1972). Statistical aspects of sea-ice ridge
442 distributions. *Journal of Geophysical Research*, *77*(30), 5954-5970.
443

444 Hibler, W.D., Mock, S.J. and Tucker, W.B. (1974). Classification and variation of sea ice ridging
445 in the western Arctic basin. *J. Geophys. Res.*, *79*(18), 2735–2743.
446

447 Hunke, E., Lipscomb, W., & Turner, A. (2010). Sea-ice models for climate study: Retrospective
448 and new directions. *J. Glaciology*, *56*(200), 1162-1172. doi:10.3189/002214311796406095

449

450 Krabill, W. B., Abdalati, W., Frederick, E. B., Manizade, S. S., Martin, C. F., Sonntag, J. G., ... &
451 Yungel, J. G. (2002). Aircraft laser altimetry measurement of elevation changes of the Greenland
452 ice sheet: Technique and accuracy assessment. *J. Geodynamics*, 34(3-4), 357-376.

453

454 Kwok, R., Kacimi, S., Markus, T., Kurtz, N. T., Studinger, M., Sonntag, J. G., et al. (2019a).
455 ICESat-2 surface height and sea ice freeboard assessed with ATM lidar acquisitions from
456 Operation IceBridge. *Geophysical Research Letters*, 46, 11,228–11,236. [https://doi.org/](https://doi.org/10.1029/2019GL084976)
457 10.1029/2019GL084976.

458

459 Kwok, R., Markus, T., Kurtz, N. T., Petty, A. A., Neumann, T. A., Farrell, S. L., et al. (2019b).
460 Surface height and sea ice freeboard of the Arctic Ocean from ICESat-2: Characteristics and early
461 results. *Journal of Geophysical Research: Oceans*, 124(10), 6942-6959.
462 <https://doi.org/10.1029/2019JC015486>.

463

464 Kwok, R., Petty, A., Cunningham, G., Markus, T., Hancock, D., Ivanoff, A., Wimert, J., Bagnardi,
465 M., Kurtz, N., & the ICESat-2 Science Team. (2021). ATLAS/ICESat-2 L3A Sea Ice Height,
466 Version 5. NASA Distributed Active Archive Center, National Snow and Ice Data Center,
467 Boulder, Colorado USA. <https://doi.org/10.5067/ATLAS/ATL07.005>.

468

469 Lowry, R. T., and P. Wadhams (1979), On the statistical distribution of pressure ridges in sea ice.
470 *J. Geophys. Res.*, 84(C5), 2487–2494, doi:10.1029/JC084iC05p02487.

471

472 MacGregor, J. A., Boisvert, L. N., Medley, B., Petty, A. A., Harbeck, J. P., Bell, R. E., et al. (2021).
473 The scientific legacy of NASA's Operation IceBridge. *Reviews of Geophysics*, 59,
474 e2020RG000712. <https://doi.org/10.1029/2020RG000712>

475

476 Magruder, L.A., Brunt, K. M. & Alonzo, M. (2020). Early ICESat-2 on-orbit Geolocation
477 Validation Using Ground- Based Corner Cube Retro-Reflectors. *Remote Sensing*, 12(21), 3653.
478 <https://doi.org/10.3390/rs12213653>.

479

480 Markus, T., Neumann, T., Martino, A., Abdalati, W., Brunt, K., Csatho, B., et al. (2017). The Ice,
481 Cloud, and Land Elevation Satellite-2 (ICESat-2): Science requirements, concept, and
482 implementation. *Remote Sensing of Environment*, 190, 260–273. <https://doi.org/10.1016/j.rse.2016.12.029>.
483
484
485 Martin, C. F., Krabill, W. B., Manizade, S., Russell, R., Sonntag, J. G., Swift, R. N., & Yungel, J.
486 K. (2012). Airborne Topographic Mapper Calibration Procedures and Accuracy Assessment.
487 NASA Technical Reports, 20120008479 (NASA/TM-2012-215891, GSFC.TM.5893.2012),
488 <http://hdl.handle.net/2060/20120008479>, 32 pp., Natl. Aeronaut. and Space Admin., Washington,
489 D. C.
490
491 Martin, T., Tsamados, M., Schroeder, D., & Feltham, D. (2016). The impact of variable sea ice
492 roughness on changes in Arctic Ocean surface stress: A model study. *Journal of Geophysical*
493 *Research: Oceans*, 121, 1931–1952. <https://doi.org/10.1002/2015JC011186>.
494
495 Neumann, T. A., Brenner, A., Hancock, D., Robbins, J., Saba, J., Harbeck, K., Gibbons, A., Lee,
496 J., Luthcke, S. B., Rebold, T., et al. (2021). ATLAS/ICESat-2 L2A Global Geolocated Photon
497 Data, Version 5. NASA Distributed Active Archive Center, National Snow and Ice Data Center,
498 Boulder, Colorado USA. <https://doi.org/10.5067/ATLAS/ATL03.005>.
499
500 Neumann, T. A., Martino, A. J., Markus, T., Bae, S., Bock, M. R., Brenner, A. C., ... & Thomas,
501 T. C. (2019). The Ice, Cloud, and Land Elevation Satellite–2 Mission: A global geolocated photon
502 product derived from the advanced topographic laser altimeter system. *Remote Sensing of*
503 *Environment*, 233, 111325. <https://doi.org/10.1016/j.rse.2019.111325>.
504
505 Parmerter, R. R., and Coon, M. D. (1972). Model of pressure ridge formation in sea ice. *J.*
506 *Geophys. Res.*, 77(33), 6565– 6575, doi:10.1029/JC077i033p06565.
507
508 Perovich, D., Meier, W., Tschudi, M., Farrell, S., Hendricks, S., Gerland, S., Kaleschke, L., Ricker,
509 R., Tian-Kunze, X., Webster, M., & Wood, K. (2019). Sea Ice. Arctic Report Card 2019, J. Richter-
510 Menge, M. L. Druckenmiller, and M. Jeffries, Eds., <http://www.arctic.noaa.gov/Report-Card>.

511
512 Roberts, A. F., Hunke, E. C., Kamal, S. M., Lipscomb, W. H., Horvat, C., & Maslowski, W.
513 (2019). A variational method for sea ice ridging in Earth system models. *Journal of Advances in*
514 *Modeling Earth Systems*, *11*, 771–805. <https://doi.org/10.1029/2018MS001395>.
515
516 Strub-Klein, L., & Sudom, D. (2012). A comprehensive analysis of the morphology of first-year
517 sea ice ridges. *Cold Regions Science and Technology*, *82*, 94-109.
518
519 Studinger, M. (2013, updated 2020). *IceBridge ATM LIB elevation and return strength, Version*
520 *2 (ILATMIB)*. NASA Distributed Active Archive Center, National Snow and Ice Data Center,
521 Boulder, Colorado, USA. <https://doi.org/10.5067/19SIM5TXKPGT>.
522
523 Tan, B., Li, Z., Lu, P., Haas, C. & Nicolaus, M. (2012). Morphology of sea ice pressure ridges in
524 the northwestern Weddell Sea in winter. *J. Geophys. Res.*, *117*, C06024, doi:
525 10.1029/2011JC007800.
526
527 Timco, G. W., & Burden, R. P. (1997). An analysis of the shapes of sea ice ridges. *Cold Regions*
528 *Science and Technology*, *25*, 65–77. [https://doi.org/10.1016/S0165-232X\(96\)00017-1](https://doi.org/10.1016/S0165-232X(96)00017-1)
529
530 Tsamados M and 7 others (2014) Impact of atmospheric and oceanic form drag on simulations of
531 Arctic sea ice. *J. Phys. Oceanog.*, *44*, 1329–1353, doi: 10.1175/JPO-D-13-0215.1.
532
533 Tschudi, M. A., Meier, W. N., & Stewart, J. S. (2020). An enhancement to sea ice motion and age
534 products at the National Snow and Ice Data Center (NSIDC). *The Cryosphere*, *14*(5), 1519-1536.
535
536 Wadhams, P., & Doble, M. J. (2008). Digital terrain mapping of the underside of sea ice from a
537 small AUV. *Geophysical Research Letters*, *35*, L01501. <https://doi.org/10.1029/2007GL031921>
538
539 Wadhams, P., & Toberg, N. (2012). Changing characteristics of arctic pressure ridges. *Polar*
540 *Science*, *6*(1), 71-77.
541

542 Wadhams, P., Tucker III, W. B., Krabill, W. B., Swift, R. N., Comiso, J. C., & Davis, N. R. (1992).
543 Relationship between sea ice freeboard and draft in the Arctic Basin, and implications for ice
544 thickness monitoring. *Journal of Geophysical Research: Oceans*, 97(C12), 20325-20334.
545
546 World Meteorological Organization (1970). Sea ice nomenclature: Terminology, codes and
547 illustrated glossary, WMO/OMM/BMO 259, TP145, World Meteorological Organization,
548 Geneva. [https://www.jcomm.info/components/com_oe/oe.php?task=download&id=](https://www.jcomm.info/components/com_oe/oe.php?task=download&id=27226&version=March%202014&lang=1&format=1)
549 [27226&version=March 2014&lang=1&format=1](https://www.jcomm.info/components/com_oe/oe.php?task=download&id=27226&version=March%202014&lang=1&format=1).